Coupled Systems Mechanics, *Vol. 7, No. 1 (2018) 79-93*
DOI: https://doi.org/10.12989/csm.2018.7.1.079

Failure analysis of ribbed cross-laminated timber plates

Marko Lavrenčič[a] and Boštjan Brank[*]

University of Ljubljana, Faculty of Civil and Geodetic Engineering, Jamova c. 2, 1000 Ljubljana, Slovenia

(Received May 9, 2017, Revised June 23, 2017, Accepted June 24, 2017)

Abstract. The process of material failure i.e. cracks development and their propagation in an experiment related to the bending collapse of cross laminated timber plate with ribs is described. Numerical simulation of such an experiment by the nonlinear finite element method is presented. The numerical model is based on Hashin failure criteria, initially developed for unidirectional composites, and on material softening concept applied by the smeared crack approach. It is shown that such a numerical model can be used for an estimation of the limit load and the limit displacement of a cross laminated timber ribbed plate.

Keywords: cross-laminated timber (CLT); ribbed timber plate; limit load analysis; Hashin failure criteria; material softening

1. Introduction

The cross laminated timber (CLT) is a building material with a lot of potential in the timber construction industry, e.g., (Brandner *et al*. 2016). From the material point of view, it is highly anisotropic, shear compliant composite laminate. In multi-storey timber buildings, the CLT is used for both horizontal and vertical structural components. When stiffened with timber ribs, it can be applied for floors with larger spans. The design of CLT structural components is based on design recommendations, technical approvals and active research, since the timber design codes do not consider yet the CLT. Despite of the considerable growth of the CLT in the world market, designers are still far from exploiting its maximum potential (Stanić *et al*. 2016). An important issue in this respect is an accumulation of knowledge related to understanding failure mechanisms of CLT structural components under different loading conditions.

The purpose of this article is to present a numerical model for failure analysis of ribbed CLT plate. The results obtained by such a model can help to understand failure mechanism of ribbed CLT plates in bending. Geometrically and material non-linearity is taken into account. The applied timber material model takes into consideration: (a) orthotropic elasticity (Reddy, 2004) (b) Hashin criteria for the initiation of material damage in tension, i.e., for the outset of crack in timber due to loading (Hashin 1980, 1981) and (c) smeared crack approach for applying material softening due to crack opening (Abaqus 2016, Ibrahimbegovic 2009).

∗Corresponding author, Professor, E-mail: bostjan.brank@fgg.uni-lj.si
[a]Ph.D. Student, E-mail: marko.lavrencic@fgg.uni-lj.si

http://www.techno-press.org/?journal=csm&subpage=8 ISSN: 2234-2184 (Print), 2234-2192 (Online)

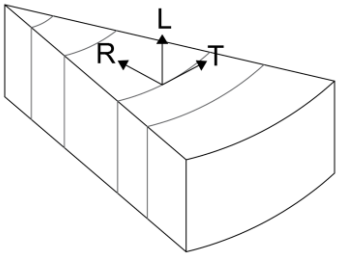

Fig. 1 Timber coordinate system

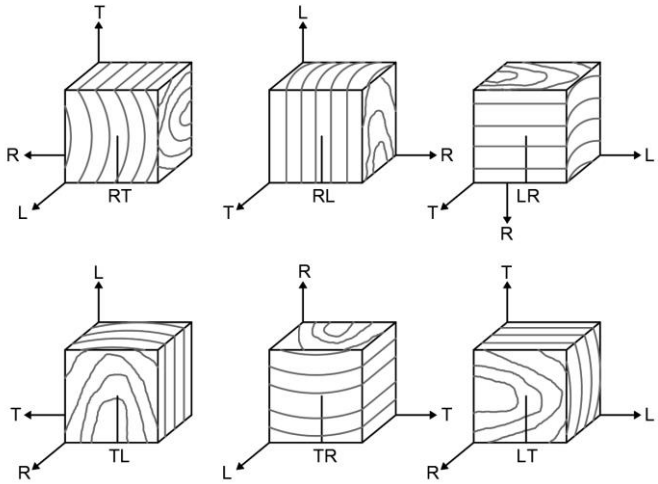

Fig. 2 Crack propagation systems in timber

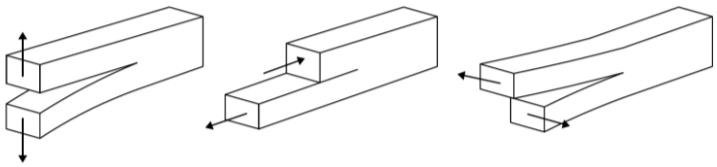

Fig. 3 Basic fracture modes (I, II and III)

For numerical simulations, a commercial finite element code for structural analysis was used (Abaqus 2016). The numerical results are compared to experimentally observed failure mechanisms of ribbed CLT plates, which are also briefly presented.

2. Cracks in timber

Timber is usually treated as an orthotropic material (Fig. 1): *L* denotes the direction of the fibers, *T* is facing tangentially to the fibers, and *R* is radial to the fibers. These labels are also used in the crack propagation system labelling, e.g., (Qiu *et al*. 2014). The first letter indicates the normal direction to the crack surface, and the second one indicates the direction of the crack propagation. In timber, six crack propagation systems, Fig. 2, are possible. In the case of bending

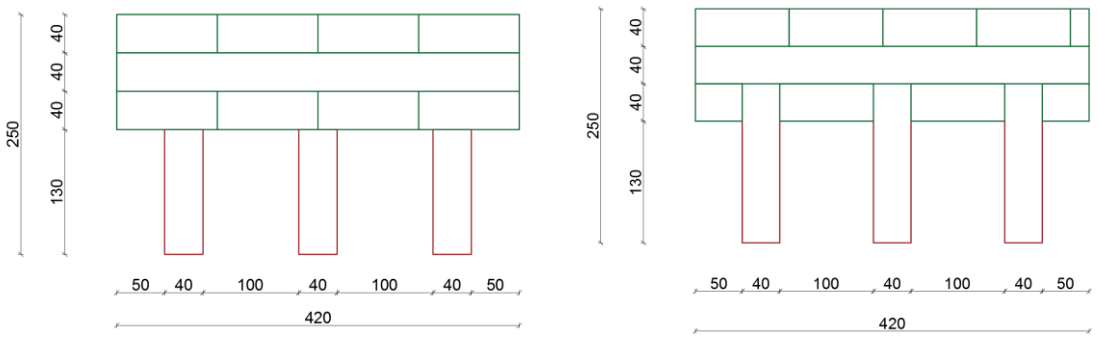

Fig. 4 Cross section of considered ribbed CLT plates (in mm). Ribs are glued to the third layer of CLT (left). Ribs and one layer of boards are glued to the second layer of CLT (right)

of the timber beam, the crack almost always extends in the direction of the fibers (*TL* and/or *RL*), where *RL* is often the critical one (Qiu *et al*. 2014); such a crack occurs without warning and spreads instantly. There are three basic fracture modes, Fig. 3: an *RL* crack, for example, can extend in modes I, II, III or in a mixed mode. A crack propagation system and a mode relate to specific fracture energy, which is the energy required for formation of a unit area of the crack. The specific fracture energy is a material constant that can be measured by specific tests, e.g., (Fruhmann *et al*. 2002).

3. Considered plates

Cross sections of considered ribbed CLT plates with length of 4 m are shown in Fig. 4. Such plates are stacked in a building one next to other and are connected to form a floor, e.g., (Brandner *et al*. 2016), which carries the load mainly in the direction of the ribs.

The upper part of considered plates is spruce CLT, classified as C24 according to (ÖNORM B 1995, 2015). The lower part consists of solid spruce ribs classified as C24; each rib may have finger joint. Two variants were used for gluing the ribs. (a) The ribs were glued to the bottom of the 3-layered CLT (Fig. 4, left); these samples were labeled 6.1.a, 6.1.b and 6.1.c. (b) The ribs were glued to the bottom of the 2-layered CLT together with one layer of boards (Fig. 4, right); these samples were labeled 3.1.a, 3.1.b and 3.1.c. The adhesive used in the CLT was polyurethane. Glue used to fix the ribs and one layer of boards in variant (b) was Purbond polyurethane, HB 110. The timber wave velocity and density were measured for the ribs and boards in order to determine the so-called dynamic elastic modulus in the direction of the fibers E_d, which is assumed to be 5% higher than the so-called static elastic modulus E_s (Machek *et al*. 2001). The average E_{s-av} for all ribs and boards used in the six aforementioned samples was 14.2 MPa (the total number of measurements was 28). ÖNORM EN 338 (2009) gives characteristic value of modulus of elasticity (at 5% fractile) and its average value for C24 spruce as $E_{0,05} = 7.4$ MPa and $E_{mean} = 11$ MPa, respectively. Thus, the coefficient of variation equals $CV(E) = 0{,}20$, and E_{s-av} corresponds to the 93% fractile for C24. Timber of the ribs and the boards was therefore of extremely high quality for C24 (according to E_{s-av} it could be C40). The average static elastic modulus for the ribs of 6.1.a and 6.1.b samples were 16.8 MPa (this could be even C50) and 11.8 MPa (this could be C27), respectively.

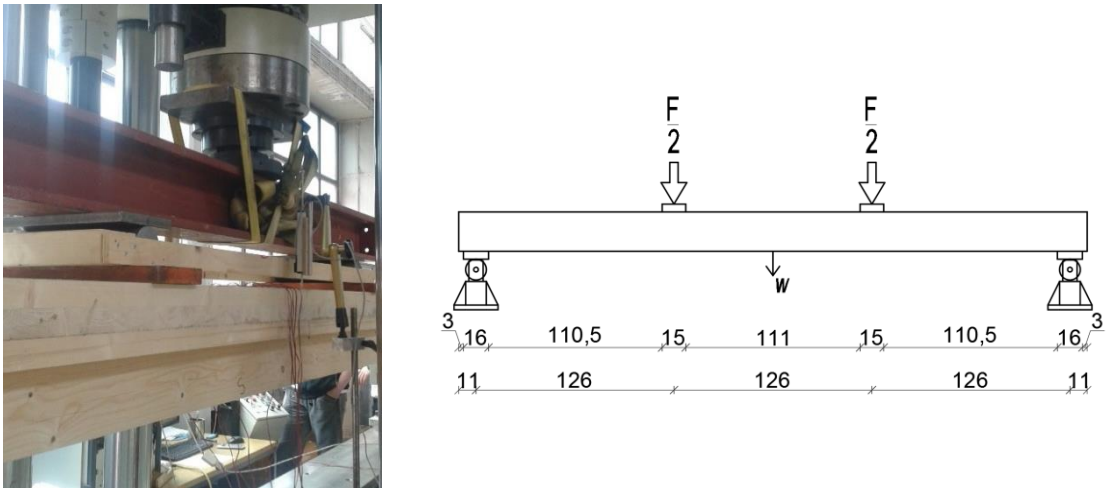

Fig. 5 Plate during the test (left); location of supports and loads (right); in cm

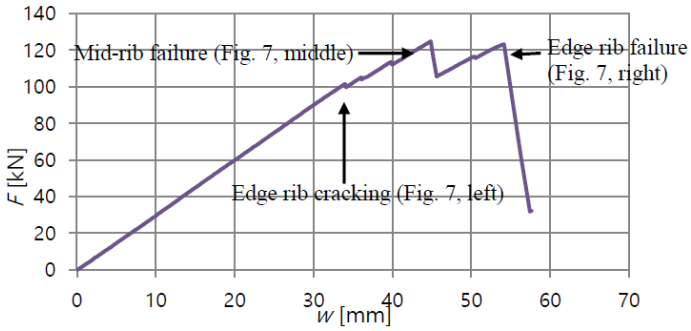

Fig. 6 Force-displacement curve for sample 6.1.a

4. Conclusion on experimental results

A bending test according to EN 408 (2012) was carried out on all six samples. The test configuration is shown in Fig. 5; velocity of the imposed piston displacement was 6 mm/min. The results below are for the sample 6.1.a (Zisi *et al*. 2016).

The relationship between the force F and the vertical displacement at the mid-span w (Fig. 5) is shown in Fig. 6. At F=101.6 kN a *RL-TL* crack of mode II (Fig. 8) appeared in the most rigid edge rib (labelled 45/9), Fig. 7 (left), leading to a small jump in the force-displacement curve. It appeared instantly and split the rib by its height. Two more similar jumps occurred in the force-displacement curve before the maximum force. They might be due to extension of the existing crack or due to formation of new cracks - this could not be verified visually. When the maximum force 124.8 kN was reached, a very prominent and long crack (*RL-TL*, modes II and III) appeared in the middle rib. The crack practically cut the rib in half longitudinally, thereby making it non-bearing, Fig. 7 (middle), which resulted in a significant drop in the force-displacement curve. After that, the plate was still able to take on a force up to 123.2 kN at w=54.1 mm, when the finger joint in the edge, previously damaged rib failed (*LT-LR*, mode I), Fig. 7 (right). This resulted in a plate collapse.

Fig. 7 Cracks in sample 6.1.a (Zisi, Aicher and Dill-Langer 2016): edge rib (left), middle rib (middle), edge rib at plate failure (right)

Fig. 8 Cracking systems *RL-TL*, modes I and II, sample 3.1.c

In failure of a ribbed CLT plate, the key role is obviously played by the *RL-TL* cracks in the ribs. The location of such cracks is random, as it depends on pre-existing cracks due to drying, knots, orientation of the annual rings, and position of the finger joint. The CLT part of the ribbed plate remains virtually intact and the same is true for the glue.

It can be concluded from this experiment (and also from the other samples) that ribbed CLT plate has an ability to collapse gradually, which is a very desirable property.

5. Hashin criteria applied for timber

Hashin (1980, 1981) derived two criteria for the crack initiation in transversely isotropic composite materials, such is, for example, polyester resin, reinforced with unidirectional glass fibers, e.g., (Brank and Makarovič 1998). Let us denote the direction of the fibers with x_1 and two orthogonal directions transverse to the fibres with x_2 and x_3 (Fig. 9). For 3d stress state, the Hashin criteria are

$$\left(\frac{\hat{\sigma}_{11}}{\sigma_A^+}\right)^2 + \frac{\hat{\sigma}_{12}^2 + \hat{\sigma}_{13}^2}{\tau_A^2} \geq 1, \qquad \text{for } \hat{\sigma}_{11} \geq 0 \tag{1}$$

$$\left(\frac{\hat{\sigma}_{22} + \hat{\sigma}_{33}}{\sigma_T^+}\right)^2 + \frac{\hat{\sigma}_{23}^2 - \hat{\sigma}_{22}\hat{\sigma}_{33}}{\tau_T^2} + \frac{\hat{\sigma}_{12}^2 + \hat{\sigma}_{13}^2}{\tau_A^2} \geq 1, \qquad \text{for } \hat{\sigma}_{nn} \geq 0 \tag{2}$$

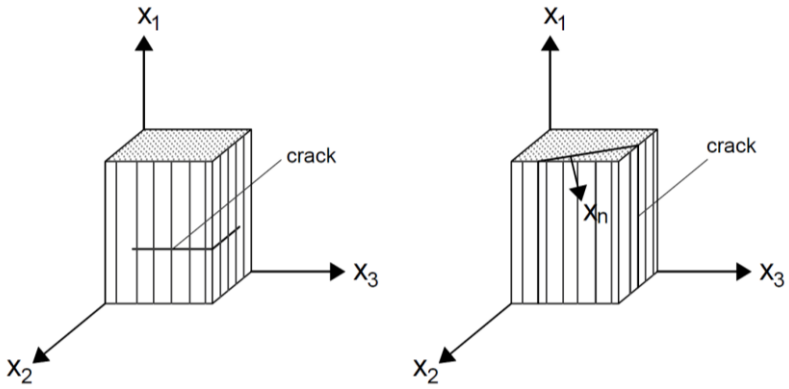

Fig. 9 Crack related to criterion (1) (left); crack related to criterion (2) (right)

where $\hat{\sigma}_{11}$, $\hat{\sigma}_{22}$ and $\hat{\sigma}_{nn}$ are normal stresses in directions x_1, x_2 and x_n, respectively, see Fig. 9 (right), σ_A^+ and σ_T^+ are tensile strengths in directions of fibers and transverse direction, respectively, τ_T and τ_A are shear strengths for shear transverse to the fibers and shear in the direction of the fibers, respectively. Criterion (1) is related to a crack opening transversely to the fibers, e.g., to the systems x_1x_2 and x_1x_3, Fig. 9 (left). The criterion (2) is related to a crack opening in the direction of the fibers, e.g., to the system x_nx_1, Fig. 9 (right). We use criteria (1) and (2) for timber.

In addition to the criteria for the crack initiation, Hashin (1980, 1981) proposed criteria for the damage initiation in compression, but these criteria are not very important for timber, since cracks have much bigger impact on the behavior of timber structure than compression damage. For 3d stress state they can be written as

$$\hat{\sigma}_{11} \geq -\sigma_A^-, \qquad \text{for } \hat{\sigma}_{11} < 0 \tag{3}$$

$$\left(\frac{\hat{\sigma}_{22}}{2\tau_T}\right)^2 + \left[\left(\frac{\sigma_T^-}{2\tau_T}\right)^2 - 1\right]\frac{\hat{\sigma}_{22}}{\sigma_T^-} + \left(\frac{\hat{\sigma}_{12}}{\tau_A}\right)^2 \geq 1, \qquad \text{for } \hat{\sigma}_{nn} < 0 \tag{4}$$

where σ_A^- and σ_T^- represent compressive strengths in direction of the fibers and direction transverse to the fibers, respectively.

When at least one of the conditions (1) or (2) is met in a material point, these signals start of cracking. During the crack propagation, fracture energy G_f is released. If Hashin criteria (1) and (2) are used for timber, a crack transverse to the fibers (Fig. 9 left) can be related to the fracture energy of systems *LT* or *LR* and a crack along the fibers (Fig. 9 right) to the fracture energy of systems *TL* or *RL*.

6. Numerical model

Due to the symmetry, only one half of the plate was modeled by using symmetry boundary conditions, Fig. 10. We used solid-shell finite elements, which externally resemble 3d finite elements, but they are based on the shell theory. Their Abaqus label is SC8R (8 nodes, 1 integration point on the middle layer and 5 integration points through the thickness). Small steel

Table 1 Used elastic and shear moduli for the CLT in MPa

E_1	E_2	G_{12}	G_{13}	G_{23}
11000	450	690	690	65

Table 2 Used ratios for softwood C24

E_2/E_1	G_{12}/E_1	G_{13}/E_1
37/1100	69/1100	69/1100

Table 3 Used strengths in MPa. Notation from Eqs. (1)-(4) is in parentheses

f_m (σ_A^+)	$f_{t,90}$ (σ_T^+)	$f_{c,0}$ (σ_A^-)	$f_{c,90}$ (σ_T^-)	f_v (τ_A)	f_r (τ_T)	$f_{t,0}^{CLT}$ (σ_A^+)	$f_{t,90}^{CLT}$ (σ_T^+)	$f_{c,0}^{CLT}$ (σ_A^-)	$f_{c,90}^{CLT}$ (σ_T^-)	f_v^{CLT} (τ_A)	f_r^{CLT} (τ_T)
67,94	0,68	44,16	4,93	6,79	6,79	23,78	0,68	35,67	5,10	3,91	1,19

plates at support and load application were modeled with elastic modulus 210 GPa and Poisson ratio 0,3. We performed non-linear analysis by using the arc-length method (Stanić *et al*. 2016, Stanić and Brank 2017).

6.1 Orthotropic material constants

To describe elastic behavior, an orthotropic material model (Reddy 2004) was used with the following material axes: x_1 (fiber direction), x_3 (thickness direction of CLT and ribs); x_1, x_2 and x_3 form a right-handed coordinate system. Note that x_1 coincides with *L*, while x_2 and x_3 coincide only approximately with *T* and *R*, respectively, Fig. 11.

Abaqus (2016) uses for SC8R condensed 3d constitutive equations due to zero normal stresses in the thickness direction, e.g., (Brank *et al*. 1997), with 6 constants: $E_1, E_2, G_{12}, \nu_{12}, G_{13}$ and G_{23}. For the CLT, we used mean values of elastic and shear moduli for C24 spruce given in ÖNORM B 1995 (2015), see Table 1, and Poisson ratio $\nu_{21} = 0{,}02$. For the ribs, we made use of the ratios between the moduli for softwood C24 according to ÖNORM EN 338 (2009), see Table 2. The moduli of each rib were obtained by multiplying these ratios to $E_s = E_1$; which were for 6.1.a sample 19725 and 16119 MPa (edge ribs), and 14523 MPa (middle rib), and for 6.1.b sample 13391 and 10018 MPa (edge ribs), and 11951 MPa (middle rib). Poisson ratio used for the ribs was the same as for the CLT. For G_{23}, we applied $G_{23} = G_{12}/10$ (ÖNORM B 1995, 2015).

6.2 Hashin criteria and used strength

Plane stress Hashin failure criteria were applied. They can be obtained by setting $\hat{\sigma}_{33} = \hat{\sigma}_{13} = \hat{\sigma}_{23} = 0$ in (1)-(4). Abaqus uses plane stress Hashin criteria and does not take into account the transverse shear stresses, although these are available for shell finite elements. The probable reason might be difficulties to accurately determine transverse shear stresses, e.g., (Brank and Carrera 2000).

Rib strengths were chosen according to ÖNORM EN 338 (2009). As E_{s-av} could be related to C40, we used the C40 mean strengths and the coefficient of variation $CV = 0{,}25$ (Brandner *et al*. 2016). Strengths of the CLT layers were according to ÖNORM B 1995 (2015); we used C24 mean strengths and $CV = 0{,}25$. The used strengths are summarized in Table 3, where f_m is bending

strength parallel to the fibers, $f_{t,90}$ is tensile strength perpendicular to the fibers, $f_{c,0}$ and $f_{c,90}$ are compressive strengths parallel and perpendicular to the fibers, respectively, and f_v and f_r are shear strengths parallel and perpendicular to the fibers, respectively.

6.3 Material softening

Abaqus (2016) models crack by material softening, which starts in the integration point if at least one of the criteria (1) and (2) is fulfilled. The fulfilment of at least one of the criteria (3) or (4) is a sign for softening due to compressive damage. Softening is governed by three parameters d_f, d_m and d_s, each running from 0 to 1. These parameters reduce the initial value of elastic and shear moduli and Poisson ratios as: $E_1 \to (1-d_f)E_1$, $\nu_{21} \to (1-d_f)\nu_{21}$, $E_2 \to (1-d_m)E_2$, $\nu_{12} \to (1-d_m)\nu_{12}$, $G_{12} \to (1-d_s)G_{12}$. It is evident that d_f is associated with fiber damage and d_m with damage transverse to the fibres. If the above expressions are applied in the plane stress constitutive matrix, (Reddy 2004), one gets

$$\boldsymbol{C}_D = \frac{1}{D}\begin{bmatrix} (1-d_f)E_1 & (1-d_f)(1-d_m)\nu_{21}E_1 & 0 \\ (1-d_f)(1-d_m)\nu_{12}E_2 & (1-d_m)E_2 & 0 \\ 0 & 0 & (1-d_s)G_{12}D \end{bmatrix} \qquad D = 1-(1-d_f)(1-d_m)\nu_{12}\nu_{21} \tag{6}$$

Matrix $\boldsymbol{C}_D$ connects stresses $\boldsymbol{\sigma} = [\sigma_{11}, \sigma_{22}, \sigma_{12}]^T$ with strains $\boldsymbol{\varepsilon} = [\varepsilon_{11}, \varepsilon_{22}, 2\varepsilon_{12}]^T$; $\boldsymbol{\sigma} = \boldsymbol{C}_D\boldsymbol{\varepsilon}$. Since the damage parameters tend towards 0, the matrix $\boldsymbol{C}_D$ reduces the material stiffness at the addressed integration point. Stresses used in the criteria (1)-(4), are additionally increased at the expense of decrease of intact material surface as

$$\hat{\boldsymbol{\sigma}} = \boldsymbol{M}\boldsymbol{\sigma}, \qquad \hat{\boldsymbol{\sigma}} = [\hat{\sigma}_{11}, \hat{\sigma}_{22}, \hat{\sigma}_{12}]^T, \qquad \boldsymbol{M} = Diag\left[(1-d_f)^{-1}, (1-d_m)^{-1}, (1-d_s)^{-1}\right] \tag{7}$$

Damage parameters from (6) are different for the tensile and compressive damage according to

$$d_f = \begin{cases} d_f^t \; if \; \hat{\sigma}_{11} \geq 0 \\ d_f^c \text{ if } \hat{\sigma}_{11} < 0 \end{cases}, \qquad d_m = \begin{cases} d_m^t \; if \; \hat{\sigma}_{22} \geq 0 \\ d_m^c \text{ if } \hat{\sigma}_{22} < 0 \end{cases}, \qquad d_s = 1-(1-d_f^t)(1-d_f^c)(1-d_m^t)(1-d_m^c) \tag{8}$$

with $d_f^t = d_1$, $d_m^t = d_2$, $d_f^c = d_3$ and $d_m^c = d_4$ related with criteria (1), (2), (3) and (4), respectively. The current value of $d_i, i = 1, \cdots, 4$, is computed from the cohesion law for criterion (i). Such a cohesive law defines relationship between stress in the crack (for $i = 1,2$) or crushing (for i = 3,4) and the opening related to the crack or crushing, see Fig. 12. From the similarity of triangles, it can be concluded from Fig. 13

$$d_i = \delta_{eq,i}^f\left(\delta_{eq,i} - \delta_{eq,i}^0\right) / \left(\delta_{eq,i}\left(\delta_{eq,i}^f - \delta_{eq,i}^0\right)\right) \tag{9}$$

where $\delta_{eq,i}$ represents the current opening. The meaning of the other notation in (9) is evident from Fig. 12. The area of the right triangle in Fig. 12 is equal to the fracture energy $G_f^{(i)}$, which is related with criteria (i). However, Abaqus (2016) requires the sum of the areas of the left and right triangle from Fig. 12 $\mathrm{G}_{\mathrm{F}}^{(i)} = A_{left}^{(i)} + G_f^{(i)}$.

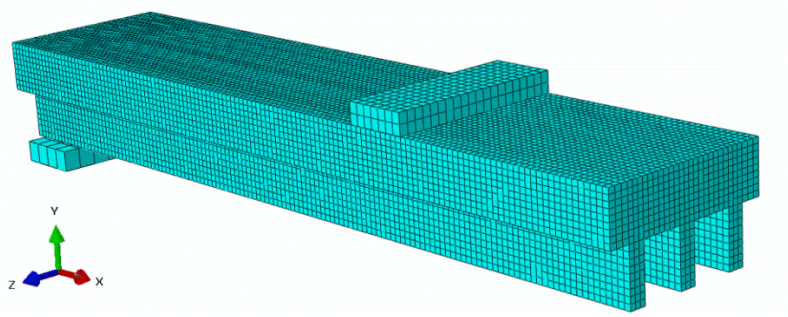

Fig. 10 Finite element mesh

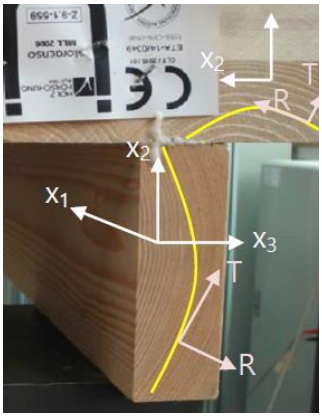

Fig. 11 *T*, *R* and x_1, x_2, x_3 coordinates in a CLT layer and in a rib

Due to the smeared crack approach, the strains are transformed into the separations $\delta_{eq,i}$ and the stresses are transformed into the tractions $f_{eq,i}$ as

$$\text{for } i=1\text{: } \delta_{eq,1} = L^C\sqrt{\langle\varepsilon_{11}\rangle^2 + \alpha\varepsilon_{12}^2}, \quad f_{eq,1} = (\langle\sigma_{11}\rangle\langle\varepsilon_{11}\rangle + \sigma_{12}\varepsilon_{12})/\left(\delta_{eq,1}/L^C\right)$$

$$\text{for } i=2\text{: } \delta_{eq,2} = L^C\sqrt{\langle\varepsilon_{22}\rangle^2 + \varepsilon_{12}^2}, \quad f_{eq,2} = (\langle\sigma_{22}\rangle\langle\varepsilon_{22}\rangle + \sigma_{12}\varepsilon_{12})/\left(\delta_{eq,2}/L^C\right) \tag{10}$$

$$\text{for } i=3\text{: } \delta_{eq,3} = L^C\langle-\varepsilon_{11}\rangle, \quad f_{eq,3} = (\langle-\sigma_{11}\rangle\langle-\varepsilon_{11}\rangle)/\left(\delta_{eq,3}/L^C\right)$$

$$\text{for } i=4\text{: } \delta_{eq,4} = L^C\sqrt{\langle-\varepsilon_{22}\rangle^2 + \varepsilon_{12}^2}, \quad f_{eq,4} = (\langle-\sigma_{22}\rangle\langle-\varepsilon_{22}\rangle + \sigma_{12}\varepsilon_{12})/\left(\delta_{eq,4}/L^C\right)$$

where L^C is characteristic length of the finite element. Computation of $f_{eq,i}$ is necessary only to the point $(\delta_{eq,i}^0, f_{eq,i}^0)$, which coincides with fullfillment of Hashin criterion (i); up to this point $d_i = 0$. All of the above is necessary in order to get mesh independent results when material softening is activated, e.g., (Ibrahimbegović 2009, Jukić *et al*. 2013).

For the computed problem, $G_f^{(1)}$ corresponds to the specific fracture energy for *LT* or *LR*, modes I or II. For Norwegian spruce $G_{f,LT,I} = 145\ \mathrm{J/m^2}$ (Dourado *et al*. 2008). Value of $G_f^{(2)}$ corresponds to the specific fracture energy for *TL*, modes I or II (and possibly also for *RL*, modes I or II). Some of the measured values are (in $\mathrm{J/m^2}$): $G_{f,TL,I} = 230$, $G_{f,RL,I} = 180$, $G_{f,RL,II} = 680$

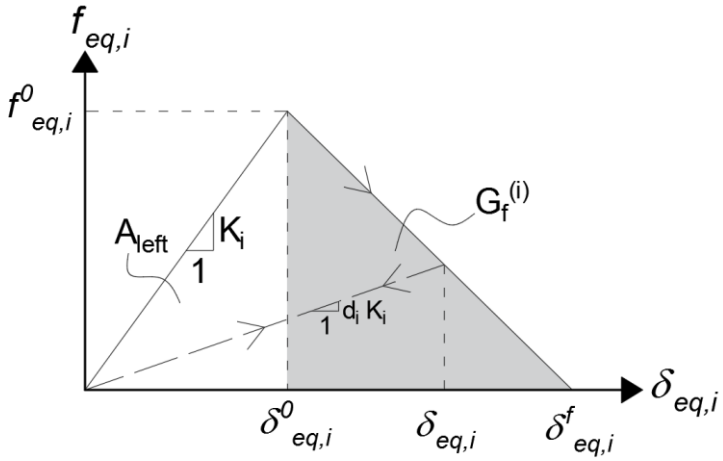

Fig. 12 Cohesive relations

for spruce (Frühmann *et al*. 2002), $G_{f,TL,I} = 248 - 309$ for Norwegian spruce (Coureau *et al*. 2013), and $G_{f,RL,I} = 260$ (Reiterer *et al*. 2000).

The values used for the numerical simulations of samples 6.1.a and 6.1.b were respectively (in $\mathrm{J/m^2}$): $\mathrm{G_F^{(1)}} = 1100$ and $\mathrm{G_F^{(1)}} = 1000$, where the area of the left triangle was estimated as $A_{left}^{(1)} \cong 850$ thus implying $G_f^{(1)} \cong 250$ and $G_f^{(1)} \cong 150$. Furthermore, we used for samples 6.1.a and 6.1.b respectively (in $\mathrm{J/m^2}$): $\mathrm{G_F^{(2)}} = 700$ and $\mathrm{G_F^{(2)}} = 500$, where the area of the left triangle was estimated as $A_{left}^{(1)} \cong 2$, thus implying $G_f^{(2)} \cong 698$ and $G_f^{(2)} \cong 498$. For the compression criteria (3) and (4) we assumed $\mathrm{G_F^{(3)}} = \mathrm{G_F^{(4)}} = 10000\ \mathrm{J/m^2}$.

7. Results of numerical simulations

For sample 6.1.a, a complete failure response was computed for the strengths from Table 3 and specific fracture energies from Section 6.3. A force-displacement curve was obtained, which was very similar to the one observed in the experiment, as shown in Fig. 13. The computed failure mechanism was also similar to the one observed in the experiment (the latter is presented in Section 4). The numerically computed failure mechanism can be observed from Figs 13 and 15: after the failure of the edge rib (A in Figs. 13 and 15), the load was carried by the middle rib and the second edge rib (B in Figs. 13 and 15), which both failed almost at the same load level (C in Figs. 13 and 15). The computed damaged locations are shown in Fig. 15. They are in good agreement with the locations of the cracks observed in the experiment. The distribution of the following damage parameters is shown in Fig. 15: d_s at A and D, d_m^t at B, and d_f^t at C. Note that Fig. 15 C shows that the tensile damage in the edge rib extends from the mid-span towards the support, which is again in agreement with the experimental crack. We can conclude that the used numerical model was able to predict nicely the limit load and the limit ductility of the specimen 6.1.a. Moreover, it was able to predict the regain of the force after the kink in the force-displacement curve in Fig. 13.

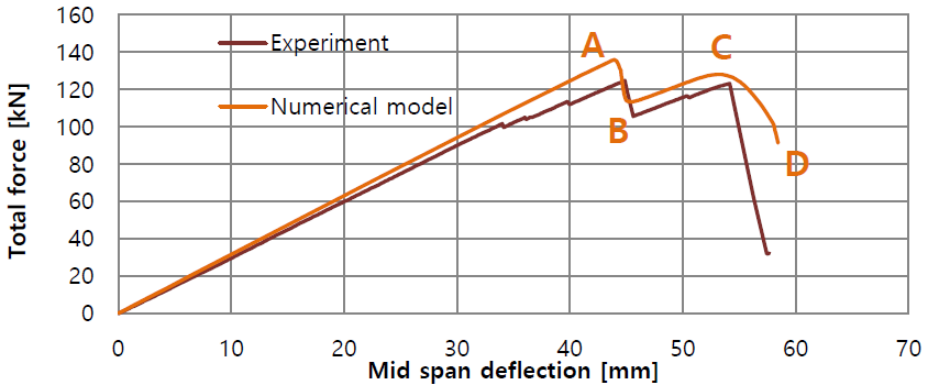

Fig. 13 Force-displacement curves for sample 6.1.a

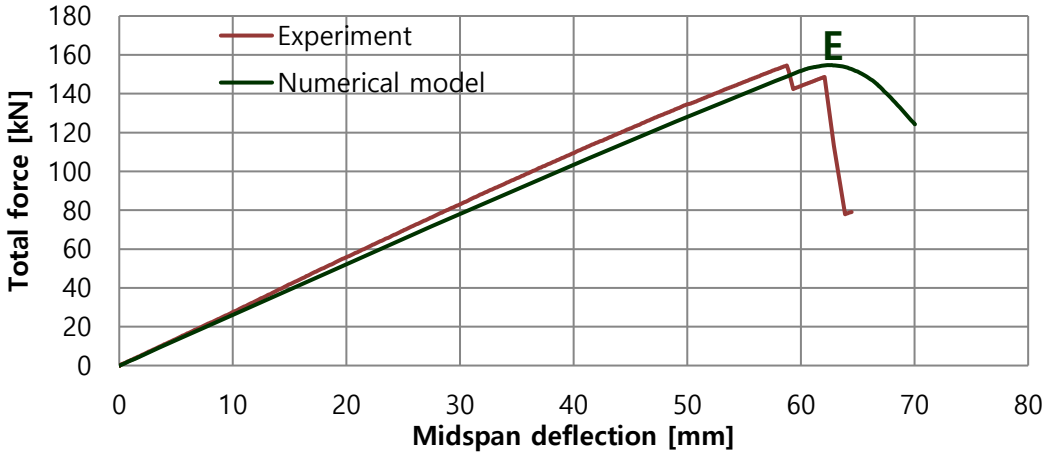

Fig. 14 Force-displacement curves for sample 6.1.b

Complete failure response was also computed for the sample 6.1.b for the strengths from Table 3 and specific fracture energies from Section 6.3. The computed limit load is in good agreement with the experimental one as shown in Fig. 14. However, for this specimen, the damage distribution predicted by the numerical model is not in a particular good agreement with the experimentally observed damage. Namely, in the experiment, the first drop in force-displacement curve (see Fig. 14) occurred due to damage in the most flexible edge rib, whereas in the numerical model, the damage first occurred in the stiffest edge rib. The reason for this may be due to a week spot in the rib or the difference between the actual orientation of the fibers and the orientation used in the model. Nevertheless, the limit load and the limit ductility were predicted nicely also for the specimen 6.1.b.

In the conclusion of this section, Fig. 16 shows results of the analyses obtained for samples 6.1.a and 6.1.b with the strengths and/or fracture energies slightly changed with respect to the data presented in Section 6. A considerable scattering of the results is evident from Fig 16. This scatter resembles the scatter of the experimental results in Fig. 17, where the load-displacement curves are presented for all six samples mentioned in Section 3. It can be seen that the scatter of experimental results is very high, in spite of classification of all used timber as C24.

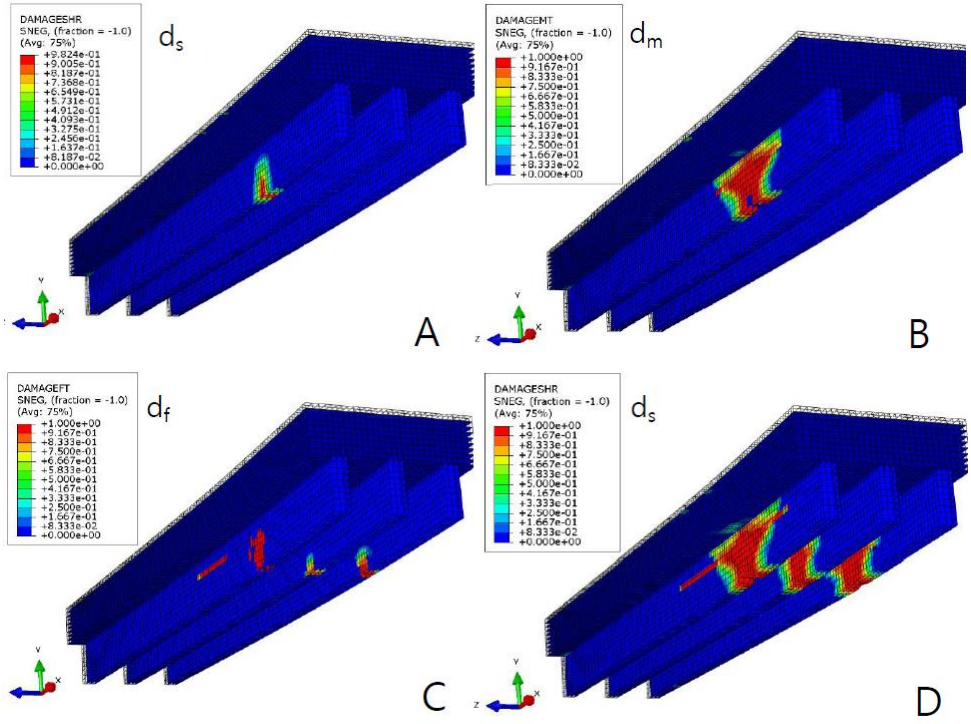

Fig. 15 Damage in the ribs for 6.1.a

8. Conclusions

Glued ribbed CLT plates will be mass-produced in the near future. It is therefore very useful to know how such plates behave in bending. As shown by the experiments (Zisi *et al*. 2016), the failure of such plates in bending is related to the appearance and propagation of large cracks in ribs. Such cracks appear in a certain sequence so that the failure of ribbed CLT plate is gradual (i.e., ductile). For that reason, the ribbed CLT plate has a substantial reserve in capacity after the occurrence of the first large longitudinal crack in one of the ribs, which is a very desirable property. For example, in the case of sample 6.1.a, the experimental limit load was 23% higher than the load at which the first major crack occurred in the edge rib. Experimental bending failure mechanism of the considered samples of ribbed CLT plates was practically the same: the ribs were cracking at certain load levels, and when the two ribs out of three failed completely due to large and wide cracks, the plate failed as well.

Many variations of the ribbed CLT plate are of course possible, depending on the CLT layer thickness, the number of CLT layers, the thickness of the ribs, the height of the ribs, the distance between the ribs, the quality of the CLT, and the quality of the timber of the ribs. In this work we considered 3 layered C24 spruce CLT and C24 spruce ribs. The thickness of the layer was 4 cm, and the ratio between the thickness, the width and the axial length of the ribs was 40/130/140. In the case of major deviations from this data a change in the failure mechanism might (or might not) be expected. We note that the detailed report on experimental results will be provided in a separate publication.

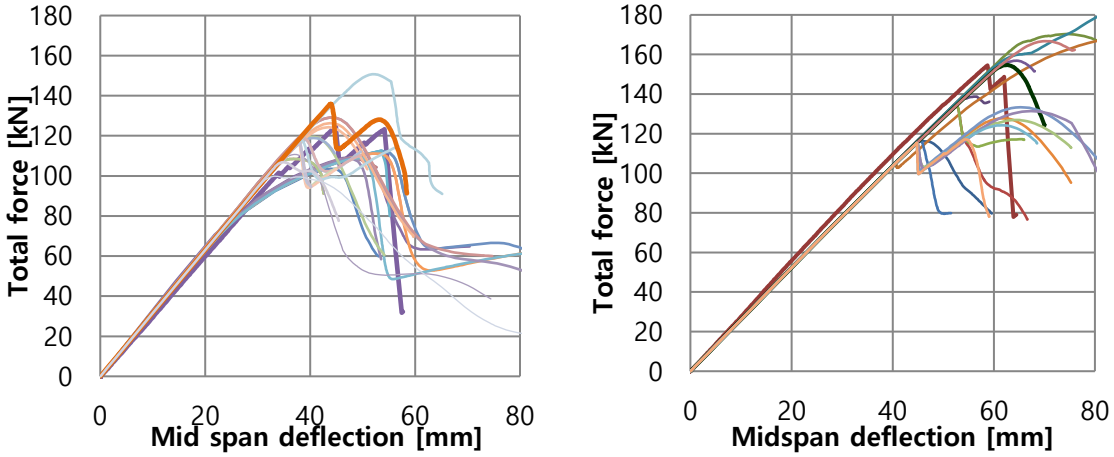

Fig. 16 Scatter of numerical results for samples 6.1.a (left) and 6.1.b (right)

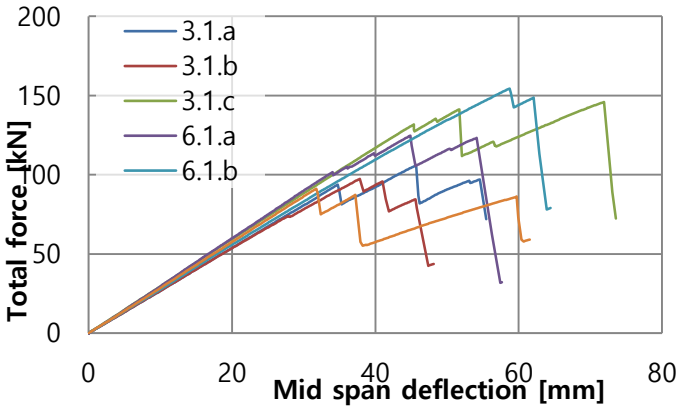

Fig. 17 Scatter of experimental results

As for numerical simulations, it has been shown that the material model based on the Hashin criteria for damage initiation and the smeared crack concept for handling the material softening can be successfully used to simulate failure analysis of timber structural elements in bending. The limit load and the limit ductility were predicted quite nice. Nevertheless, we do not really recommend too much such a model for wide use due to its sensitivity to the (relatively) small changes in strengths, fracture energies and the way the load is applied. It seems that methods which simulate the formation and propagation of cracks in the material, e.g., X-FEM and embedded discontinuity FEM, see e.g., (Dujc *et al*. 2010, 2010, 2013), (Piculin *et al*. 2016) are more appropriate, but they are still poorly developed for the use with timber structural components.

Acknowledgments

The work was financially supported by WoodWisdom-Net+ and the Ministry of Science,

Higher Education and Sport of the Republic of Slovenia. The authors thank Dr. Nikola Zisi and Jaka Brezočnik, who conducted the experiments, Sara Piculin, who performed initial numerical analysis, Iztok Šušteršič for helpful discussions and partners of the HCLTP project.

References

Abaqus (2016), *Abaqus Manuals*, Dassault Systemes, Providence, RI, U.S.A.

Brandner, R., Flatscher, G., Ringhofer, A., Schickhofer, G. and Thiel, A. (2016), "Cross laminated timber (CLT): Overview and development", *Eur. J. Wood Prod.* **74**, 331-351.

Brank, B. and Carrera, E. (2000), "Multilayered shell finite element with interlaminar continuous shear stresses: A refinement of the Reissner-Mindlin formulation", *J. Numer. Meth. Eng.*, **48**, 843-874.

Brank, B. and Makarovič, M. (1998), "On non-linear response of polyester tanks: Comparison of experimental and numerical results", *Proceedings of the NATO Advanced Research Workshop on Multilayered and Fibre-Reinforced Composites: Problems and Prospect*, Kiev, Ukraine, June.

Brank, B., Perić, D. and Damjanić, F.B. (1997), "On large deformations of thin elasto-plastic shells: Implementation of a finite rotation model for quadrilateral shell element", *J. Numer. Meth. Eng.*, **40**, 689-726.

Coureau, J.L., Morel, S. and Dourado, N. (2013), "Cohesive zone model and quasibrittle failure of wood: A new light on the adapted specimen geometries for fracture tests", *Eng. Fract. Mech.*, **109**, 328-340.

Dourado, N., Morel, S., De Moura, M.F.S.F., Valentin, G. and Morais, J. (2008), "Comparison of fracture properties of two wood species through cohesive crack simulations", *Compos.: Part A*, **39**, 415-427.

Dujc, J., Brank, B. and Ibrahimbegović, A. (2013), "Stress-hybrid quadrilateral finite element with embedded strong discontinuity for failure analysis of plane stress solids", *J. Numer. Meth. Eng.*, **94**, 1075-1098.

Dujc, J., Brank, B. and Ibrahimbegović A. (2010), "Quadrilateral finite element with embedded strong discontinuity for failure analysis of solids", *Comput. Model. Eng. Sci.*, **69**, 223-259.

Dujc, J., Brank, B. and Ibrahimbegovic, A. (2010), "Multi-scale computational model for failure analysis of metal frames that includes softening and local buckling", *Comput. Meth. Appl. Mech. Eng.*, **199**, 1371-1385.

EN 408:2010+A1 (2012), *Timber Structures-Structural Timber and Glued Laminated Timber-Determination of Some Physical and Mechanical Properties*, European Committee for Standardization (CEN).

Frühmann, K., Reitererz, A., Tschegg, E.K. and Stanzl-Tschegg, S.S. (2002), "Fracture characteristics of wood under mode I, mode II and mode III loading", *Philosoph. Mag. A*, **82**, 3289-3298.

Hashin, Z. (1980), "Failure criteria for unidirectional fiber composites", *J. Appl. Mech.*, **47**, 329-334.

Hashin, Z. (1981), "Fatigue failure criteria for unidirectional fiber composites", *J. Appl. Mech.*, **48**, 846-852.

Ibrahimbegović, A. (2009), *Nonlinear Solid Mechanics*, Springer Netherlands, Dordrecht, the Netherlands.

Jukić, M., Brank, B. and Ibrahimbegović, A. (2013), "Embedded discontinuity finite element formulation for failure analysis of planar reinforced concrete beams and frames", *Eng. Struct.*, **50**, 115-125.

Machek, L., Militz, H. and Sierra-Alvarez, R. (2001), "The use of an acoustic technique to assess wood decay in laboratory soil-bed tests", *Wood Sci. Technol.*, **34**, 467-472.

ÖNORM B 1995-1-1: Eurocode 5 (2015), *Design of Timber Structures-Part 1-1: General-Common rules and Rules for Buildings-National Specifications for the Implementation of ÖNORM EN 1995-1-1, National Comments and National Supplements*, Austrian Standards Institute.

ÖNORM EN 338:2009-10 (2009), *Structural Timber-Strength Classes*, Austrian Standards Institute.

Piculin, S., Nicklisch, F. and Brank, B. (2016), "Numerical and experimental tests on adhesive bond behaviour in timber-glass walls", *J. Adhes. Adhes.*, **70**, 204-217.

Qiu, L.P., Zhu, E.C. and Van De Kuilen, J.W.G. (2014), "Modeling crack propagation in wood by extended finite element method", *Eur. J. Wood Prod.*, **72**, 273-283.

Reddy, J.N. (2004), *Mechanics of Laminated Composite Plates and Shells: Theory and Analysis*, CRC Press,

Boca Raton, Florida, U.S.A.
Reiterer, A., Stanzl-Tschegg, S.E. and Tschegg, E.K. (2000), "Mode I fracture and acoustic emission of softwood and hardwood", *Wood Sci. Technol.*, **34**, 417-430.
Schmidt, J. and Kaliske, M. (2009), "Models for numerical failure analysis of wooden structures", *Eng. Struct.*, **31**, 571-579.
Stanić, A. and Brank, B. (2017), "A path-following method for elasto-plastic solids and structures based on control of plastic dissipation and plastic work", *Fin. Elem. Analy. Des.*, **123**, 1-8.
Stanić, A., Brank, B. and Korelc, J. (2016), "On path-following methods for structural failure problems", *Comput. Mech.*, **58**, 281-306.
Stanić, A., Hudobivnik, B. and Brank, B. (2016), "Economic-design optimization of cross laminated timber plates with ribs", *Compos. Struct.*, **154**, 527-537.
Zisi, N., Aicher, S. and Dill-Langer, G. (2016), *Testing of Specimen 6.1.a*, Internal HCLTP Report, MPA, Stuttgart, Germany.

AI